LAWRENCE
LIVERMORE
NATIONAL
LABORATORY

UCRL-TR-228796

INTRACELLULAR CHEMICAL MEASUREMENTS:A GENERALIZED APPROACH WITH HIGH-SPATIAL RESOLUTION USING FUNCTIONALIZED NANOPARTICLES

T. Laurence

March 8, 2007

This work was performed under the auspices of the U.S. Department of Energy by University of California, Lawrence Livermore National Laboratory under Contract W-7405-Eng-48.

FY06 LDRD Final Report

INTRACELLULAR CHEMICAL MEASUREMENTS: A GENERALIZED APPROACH WITH HIGH-SPATIAL RESOLUTION USING FUNCTIONALIZED NANOPARTICLES

LDRD Project Tracking Code: 03-ERI-010

Ted Laurence, Principal Investigator

Abstract

We are developing an alternative approach to optical probes that will ultimately allow us to measure chemical concentrations in microenvironments within cells and tissues. This approach is based on monitoring the surface-enhanced Raman scattering (SERS) response of functionalized metal nanoparticles (50-100 nm in diameter). SERS allows for the sensitive detection of changes in the state of chemical groups attached to individual nanoparticles and small clusters. We present the development of a nanoscale pH meter. The pH response of these nanoprobes is tested in a cell-free medium, measuring the pH of the solution immediately surrounding the nanoparticles. We developed and used SERS correlation spectroscopy and single particle/cluster SERS spectroscopy to characterize heterogeneities in the SERS signal, which result from the formation of small nanoparticle clusters. These heterogeneities have historically provided inconsistent response to pH, leading a poor sensitivity of ~1 pH unit. The response of the nanoscale pH meters is tested under a wide range of conditions to approach the complex environment encountered inside living cells and to optimize probe performance. We have also developed a rapid scanning technique to obtain pH information using confocal microscopic imaging. Together with the development of hollow gold nanoshells with collaborators, this project enables future cell-based studies of pH using SERS. This research will be continued as a collaboration with the Center for Biophotonics Science and Technology (CBST) at UC Davis Medical Center.

This work was performed under the auspices of the U. S. Department of Energy (DOE) by the University of California, Lawrence Livermore National Laboratory (LLNL) under Contract No. W-7405-Eng-48. The project 03-ERI-010 was funded by the Laboratory Directed Research and Development Program at LLNL.

Background

Recent research has shown that chemical microenvironments play a crucial role in both normal and diseased tissues. Measuring chemical concentration variations or chemical gradients across membranes is important for understanding basic biological processes, and relevant to developing disease treatments. High spatial resolution is essential for measuring chemical concentrations in small microenvironments such as cells. In order to understand the role of these chemical microenvironments, we need tools that are capable of providing chemically specific information along with sufficient spatial resolution. Much of the data on chemical microenvironments was acquired using

magnetic resonance imaging. For example, magnetic resonance spectroscopy (MRS) has been used extensively to measure the intracellular and extracellular pH of tumors in cell-based studies as well as *in vivo*, monitoring tumor development in mice[1]. While MRS has been useful in identifying the presence of chemical microenvironments, the spatial resolution is limited to 0.1 to 1 mm. It is speculated that microenvironments are present on a much smaller scale prompting the need for higher resolution techniques for measuring chemical concentrations in these microenvironments.

Optical probes have been developed that can provide spatial resolution on the order of a micron. These probes are based on a variety of fluorescent dyes that change their fluorescent properties in response to chemical changes in their environment. For example, the dye fluorescein exhibits a sensitivity to pH, which changes both fluorescence lifetime and the spectral emission of the dye [2]. These dyes, however, have a number of shortcomings: organic dyes rapidly photobleach under continuous excitation, limiting the observation time to typically about a few minutes. Also, the fluorescent dyes are generally used at very high concentrations in order to detect the signal over the autofluorescence background of the cell. This can significantly alter the chemistry within cells, and increases the risk of toxicity of the fluorescent dyes.

Raman Spectroscopy uses specific, narrow lines caused by molecular vibrational modes to identify chemical groups and their states [3]. This is a great benefit for chemical identification; however, Raman signals are too weak to detect on the single-molecule or single-particle level. Also, there is no ability to select for particular analytes: in a heterogeneous environment, many molecules will contribute to the Raman signal. However, if the chemical group of interest is near a metal surface with a roughness on the nanometer scale, an enormous enhancement of the signal occurs, resulting in detectable signals from single particles. This phenomenon is known as Surface-Enhanced Raman Spectroscopy (SERS) [4]. If the excitation is resonant with an electronic transition in the molecule, then Raman signals from single molecules may even be detected [5].

In order to overcome the limitations of MRS, fluorescence spectroscopy, and Raman spectroscopy for monitoring analyte concentrations in heterogeneous environments, we are currently developing a new generation of intracellular probes based on the surface-enhanced Raman scattering (SERS) of analyte-sensitive molecules attached to gold or silver nanoparticles. These nanoparticle probes will enable us to monitor the analyte concentration inside the highly heterogeneous chemical environment of cells and tissues with diffraction limited spatial resolution for extended periods of time. The signal strength allows detection of single particles or clusters, and the signal show little or no photodegradation with time. Individual nanoparticles/clusters can be imaged with confocal microscopy to obtain position information with diffraction-limited resolution. Moreover, the location of the nanparticles within the cell can be pinpointed to within 10nm by fitting the intensity profile [6].

Accomplishments

During this project, we made several methodological improvements that have been used to improve our understanding of the physics of the SERS pH nanoprobes. These insights have helped in testing newly developed hollow gold nanoshells [7, 8]. These nanoshells will now be used in combination with the fast confocal imaging we have developed to perform cell-based measurements of local pH.

Papers

SPIE Proceedings, 2004

UCRL-PROC-207711
This conference proceedings paper provides an overview of some of our methodological improvements, and serves as a basis for two manuscripts in preparation.

The following three articles were partially supported by this grant. The single molecule and correlation analysis developed in these articles were intended both for fluorescence applications (as shown in these papers) and for the SERS. The application of this methodology to SERS is detailed in two manuscripts in preparation.

PNAS, 2005

UCRL-JRNL-208639

Optics Letters, 2006

UCRL-JRNL-216336

Biophysical Journal, 2007

UCRL-JRNL-222408

Manuscripts in preparation:

Excerpt from "SERS correlation spectroscopy – solution-based characterization of single scattering centers"

Very strong enhancement of Raman scattering in SERS is correlated with formation of aggregates or clusters. These enhancements result from the intense electric fields located at the junctions of the nanoparticle aggregates. Unfortunately, heterogeneity of cluster formation leads to heterogeneity in enhancements. The heterogeneity reduces the ability to use SERS in a well-controlled manner for practical applications. Recently, nanoshells [7, 8] have been introduced that reduce the variability in the pH response of nanoparticles.

For preliminary characterization, a high-throughput method is needed. In order to test changes in nanoparticles that may improve the heterogeneity, many samples will need to be tested in similar conditions. The standard practice of placing particles on the surface, and performing spectroscopy particle by particle yields a large amount of information on individual particles. However, only a small number of particles is generally probed. Time resolution is generally very limited, down to 30-100 ms at best.

An alternative approach to characterizing the spectroscopic properties of nanoparticle systems is to use solution based techniques. Solution-based techniques have been used for several years in fluorescence studies. In single-molecule fluorescence studies (SMFS), immobilized molecules provide long-time trajectories on the order of several tens of seconds. Solution-based studies contain less information per molecule, but are able to easily probe up to thousands of molecules, easily characterizing any subpopulations. In an analogous fashion to SMFS, here we use solution-based methods

to characterize nanoparticles diffusing in solution. Experiments are similar to Eggeling et al [9] with the omission of the lifetime spectroscopy and the addition of multiple channels monitoring narrow spectral ranges. To date, the solution based characterization of nanoparticles has focused on correlation spectroscopy over relatively wide spectral ranges. Here, we quantify the relative contributions of Rayleigh, Raman, and continuum background scattering using ratiometric variables and correlation spectroscopy. These techniques are shown to be effective tools in characterizing distributions of scattering particles. By comparing solid spherical gold nanoparticles of a uniform size (within 10%), silver nanoparticles of varying size and shape, and uniform hollow gold nanoshells, we show that the behavior of the scattering particles depends strongly on shape and composition. The changes in behavior are likely explained by variations in plasmon resonance shapes from particle to particle or particle cluster to particle cluster. The excitation intensity dependence of these processes are shown to be linear in the excitation power range relevant for single particle studies (case we are considering).

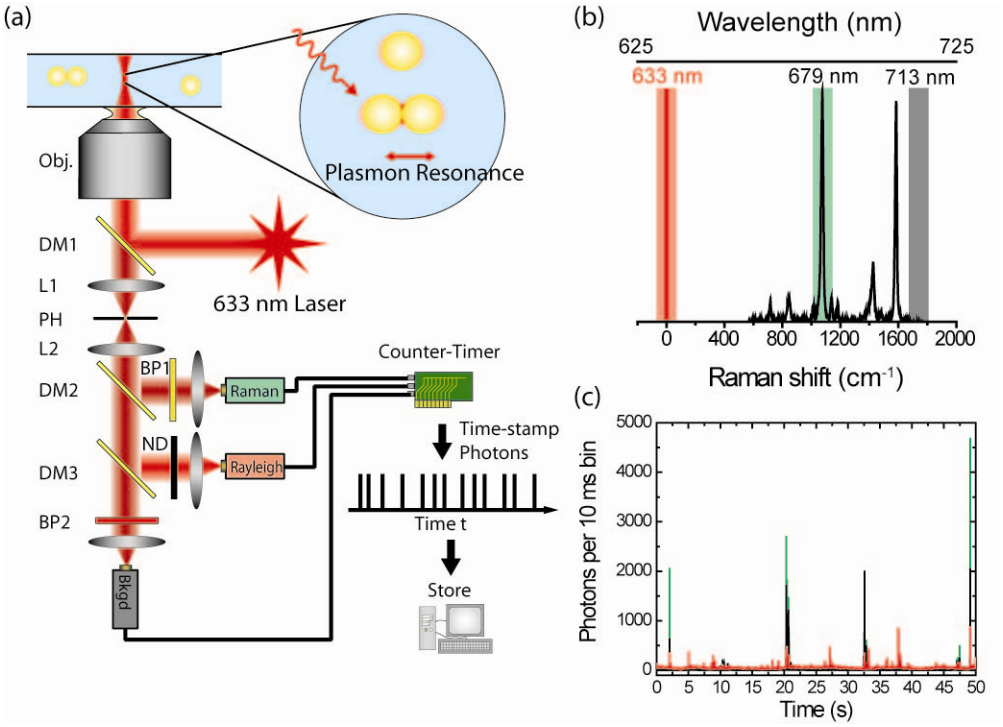

Figure 1: (a) Experimental setup for ratiometric single particle and cluster SERS spectroscopy. Individual metallic nanoparticles and clusters of nanoparticles are allowed to freely diffuse in solution. Excitation light from a 633 nm HeNe laser is reflected by a dichroic mirror (DM1, dual band dichroic reflecting 488 nm and 633 nm, Omega Optical). The laser excitation is focused into solution by a high numerical aperture microscope objective (1.4 NA oil immersion, Nikon), and bursts of photons scattered by diffusing nanoparticle clusters are collected by the same objective. After passing through DM1, the tube lens (L1) focuses the scattered light onto a pinhole (PH) to exclude out of focus light. The scattered light is then collimated using an achromatic lens (L2). Two successive dichroic mirrors (DM2 and DM3) split the scattered light into three spectral domains. Bandpass filter 1 (BP1, 679DF6, Omega Optical) selects for the 1055 cm^{-1} Raman line of 4-

mercaptobenzoic acid (MBA; green detector). BP2 (713DF6, Omega Optical) selects a small spectral region without any Raman line for MBA (gray detector); this channel monitors the strength of the continuum background. A third channel has an OD 3.0 neutral density filter and monitors the Rayleigh scattering from the particles (red detector). Photons detected by avalanche photodiodes (APDs, SPCM-AQR-14, PerkinElmer Optoelectronics) send TTL pulses to the counter timer card (PCI-6602, National Instruments) which records them with 12.5 ns time resolution, and stores them in the computer. (b) SERS spectrum of MBA on Ag nanoparticles overlaid with spectral ranges selected by filters for the three detectors. (c) Time trace with 10 ms time resolution showing individual Au nanoparticle scattering centers traversing the optical detection volume. The three channels shown correspond to the three detectors in part (a): green for the Raman line, black for the continuum background, and red for Rayleigh scattering. As can be seen, signal strength is often very strong, with thousands of photons detected per single burst.

Individual scattering nanoparticles or clusters diffuse through the confocal detection volume defined by the focused laser and the pinhole in the experimental setup described in figure 1. The scattered light is simultaneously monitored using three channels, corresponding to a Raman line, the Rayleigh line, and a section of continuum background scattering. These three detectors and the associated timing electronics are used to record arrival times of scattered photons with 12.5 ns resolution, forming three photon streams, $I_{\mathrm{Rm}}(t)$, $I_{\mathrm{Ry}}(t)$, and $I_{\mathrm{Bkgd}}(t)$. These photon streams are analyzed by searching for photon bursts and calculating ratiometric observables, as well as performing auto- and cross-correlation analyses.

A burst of scattered photons from individual scattering clusters or particles is found using the algorithm described in [10], and provides start and end times t_{start} and t_{end}. The number of photons from each channel is integrated over this time: $N_{\mathrm{Rm}} = \int_{t_{\mathrm{start}}}^{t_{\mathrm{end}}} I_{\mathrm{Rm}}(t)\,dt$, similar definitions for N_{Ry} and N_{bkgd}. Two ratiometric variables quantify the relative intensities of the Rayleigh, Raman, and continuum background scattering. First,

$$r_{Ry} = N_{\mathrm{Rm}} \Big/ \left(N_{\mathrm{Ry}} + N_{\mathrm{Rm}} \right) \tag{1}$$

which gives the fraction of photons detected that are from Rayleigh scattering vs. Raman scattering and continuum background scattering (note that the Rayleigh scattering APD had a neutral density filter with OD 3.6). Second,

$$r_{\mathrm{bkgd}} = N_{\mathrm{Rm}} \big/ N_{\mathrm{bkgd}} + N_{\mathrm{Rm}} \tag{2}$$

which gives the fraction of photons that come from the “background” channel that does not contain a Raman line for MBA, ignoring the Rayleigh scattering.

Both r_{Ry} and r_{bkgd} are expected to increase upon functionalization of the nanoparticles with MBA relative to the increasing contributions from Raman scattering. (They could, however, also be affected by aggregation after MBA addition – should show a before and after comparison of just background and Rayleigh). Note that the Raman

channel also contains a contribution from continuum background scattering, so that this ratio cannot be 0 in the absence of MBA.

Correlation Spectroscopy

Correlation spectroscopy on SERS, background scattering, and Rayleigh scattering signals of nanoparticles provides rotational and translational diffusion parameters of particles. These can be interpreted in terms of the size of the scattering particles and clusters. As we will see, it will also allow us to distinguish between anisotropic scattering from particle-particle junctions and more isotropic scattering from individual nanoshells.

A modification of the experimental setup in figure 1 is used to probe the origin of the two-time scale behavior found in correlations. Only two APDs are used, and a polarizing beam splitter cube is used rather than dichroic mirrors. The initial polarization of the laser beam is now carefully chosen to be linear. Polarization-FCS measures a polarization response and rotational diffusion times

Ratiometric Single-cluster spectroscopy monitors SERS and Rayleigh Scattering

We first characterized the nanoparticle scattering properties using the ratios r_{Ry} and r_{bkgd}, which are both ratios expected to increase as the concentration of MBA is increased. Figure 2 shows two-dimensional histograms showing the number of photon bursts as a function of r_{Ry} and r_{bkgd} for the solid Ag, solid Au, and Au nanoshell samples. These histograms show a more homogeneous response for the Au nanoshell samples than for the solid Ag or Au samples.

The Ag nanoparticles used in this study are not of uniform size or shape, but they have been frequently used in studies showing very large Raman enhancements[5]. Without addition of any MBA, observing an aliquot of the original sample, we observe a large number of scattering centers with significant Rayleigh scattering, and relatively little Raman scattering or continuum background scattering. This is shown by the large number of bursts with r_{Ry} near 0 in Fig. 2a. Even so, there are a significant number of scattering particles that show large signals ($r_{Ry}>0$) in the Raman and Continuum Background channels. This suggests that the presence of the attached Raman-active molecule is not necessary to see continuum background scattering; however, this does not exclude the possibility that the Raman-active molecule enhances the continuum background. With the addition of 10 μM MBA in Fig. 2b, a new subpopulation emerges in the upper right-hand corner of the plot, with high r_{Ry} and r_{bkgd}. The scattering in this subpopulation is dominated by the SERS signal from MBA on the surface. As more MBA is added (Fig. 2c), aggregation of the nanoparticles increases greatly (shown below), and the SERS signal increases.

The Au nanoparticles are of much more uniform size and shape. In the sample without added MBA (Figure 2d), there are two subpopulations visible: one with very little Raman or Continuum Background scattering (low r_{Ry}), and one with significant Raman or CB scattering (r_{Ry} between 0.7 and 1.0). When MBA is added (Figures 2e and 2f), the position of the peak showing Raman or CB scattering shifts to higher r_{bkgd}. This

is because the Raman line from MBA now appears, and the intensity in the channel monitoring that line increases. The increase is not as dramatic in this case as in the case with Ag. This is expected, since Ag in general provides larger SERS enhancements.

For the Au nanoshells (Fig. 2g-i), r_{bkgd} increases with MBA as with the solid nanoparticles. However, one large difference is that there is only one subpopulation visible. The distribution in r_{Ry} is relatively wide, but it does not split into two distinct subpopulations. This is likely due to the more homogeneous nature of the scattering nanoshells.

In order to see a significant scattering signal from a nanoparticle, the electric field at the particle E_{part} must be enhanced compared to the free electric field E_{free} both at the laser excitation frequency ω_0 and at the Raman-shifted frequency $\omega_0 - \Delta$, $\frac{\left|E_{\text{part}}(\omega_0)\right|^2}{\left|E_{\text{free}}(\omega_0)\right|^2}\frac{\left|E_{\text{part}}(\omega_0-\Delta)\right|^2}{\left|E_{\text{free}}(\omega_0-\Delta)\right|^2}$ [11]. Due to the relatively wide plasmon resonance of nanoshells, Raman scattering from individual nanoshells is visible. However, Plasmon resonances of individual solid Ag and Au nanoparticles are not wide enough to capture the laser wavelength of 633 nm and the Raman shifted wavelength. In order to obtain detectable signals in these cases, inter-particle junctions are necessary, allowing for wider Plasmon resonaces. Such Plasmon resonances of inter-particle junction are not as well-controlled as in nanoshells, leading us to expect wider distributions in the ratios r_{Ry} and r_{bkgd}. We understand the large population of solid nanoparticles with low r_{Ry} to be particle aggregates that showed strong plasmon resonances at ω_0, but much weaker at $\omega_0 - \Delta$. The nanoshells showed a more uniform response because of the better control over the Plasmon resonance.

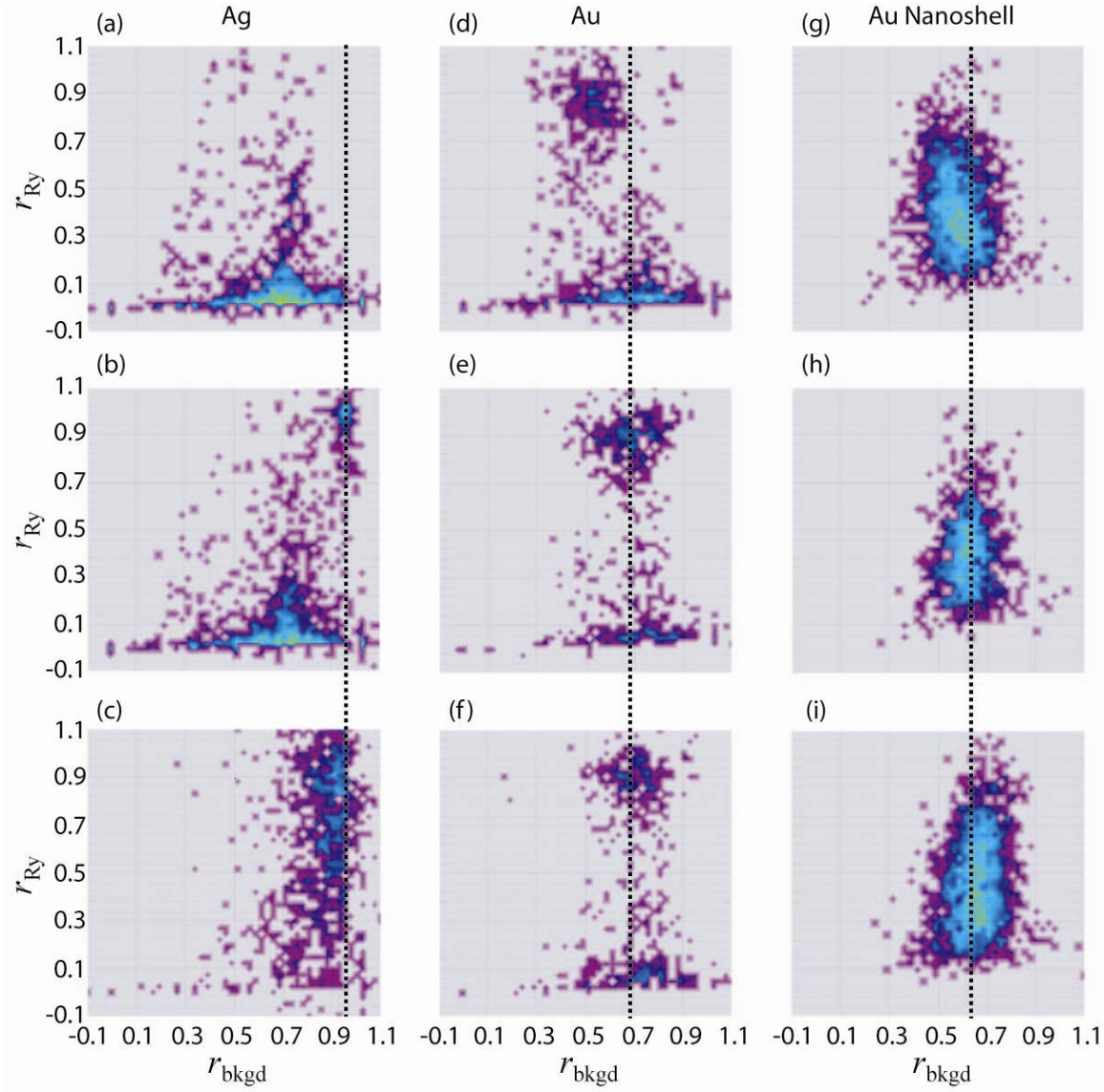

Figure 2: Ratiometric variables r_{Ry} and r_{bkgd} calculated for single diffusing clusters or particles are used to monitor the effects of functionalizing the nanoparticles with 4-mercaptobenzoic acid (MBA). Histograms for Ag nanoparticles formed using citrate reduction according to Lee and Meisel with 0, 10, and 50 μM MBA are shown in (a), (b), and (c), respectively. Histograms for gold nanoparticles (size, synthesis) with 0, 10, and 50 μM MBA are shown in (d), (e), and (f), respectively. Histograms for gold nanoshells (size, synthesis) with 0, 50, and 500 μM MBA are shown in (g), (h), and (i), respectively. The dotted lines indicate the position in r_{bkgd} of the Raman active subpopulation at the intermediate MBA concentration for each substrate. Clearly, the position of Raman active subpopulation shifts to the right as MBA is added. Inducing aggregation by adding NaCl does causes a smaller shift in the opposite direction (data not shown).

In Figure 3, we examine the widths of the distributions from Figure 2 more quantitatively, showing that the nanoshells produce narrower distributions in r_{Ry} and r_{bkgd}. In Figures 2a-c, one dimensional histograms are shown for all bursts with a large Raman component. Note that the widths of the histograms for nanoshells are narrower, especially after adding MBA. r_{bkgd} is highest for Ag, consistent with the fact that it gives the largest SERS signals. Histograms from Ag are also most erratic, probably due to uncontrolled shape. Wide histograms for 50 μM added to Ag are due to aggregation.

In Figure 2e-f, we show the mean and standard deviation of the ratios r_{Ry} and r_{bkgd} for all bursts, without selection of large Raman signals. In these plots, we see that the response of the nanoshells is much more homogeneous, with lower standard deviation in all cases. Even if we select only those bursts that show a larger Raman signal (Figure 2f), the widths of the histograms for the nanoshells are lower, once MBA is added. Note that the narrowing of the distribution for Ag at higher MBA concentrations is due simply to the high value of the ratio r_{bkgd} [12].

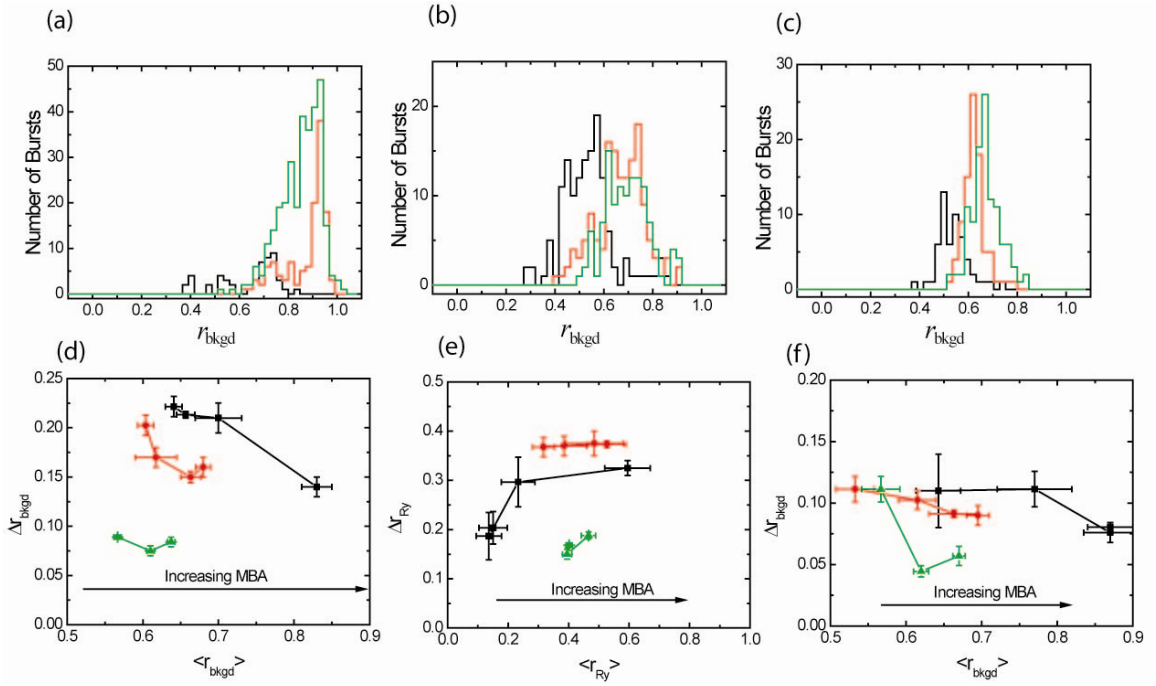

Figure 3: Histograms of ratiometric variables r_{bkgd} calculated for single diffusing clusters with bright Raman signal (>15 kHz) selected from histograms in figure 2. (a) Histograms for Ag nanoparticles with 0 (black), 10 (red), and 50 μM MBA (green). (b) Histograms for gold nanoparticles with 0 (black), 10 (red), and 50 μM MBA (green). (c) Histograms for gold nanoshells with 0 (black), 50 (red), and 500 μM MBA (green). (d) Fitted peak position and width for histograms of r_{bkgd} from figure 2. For Ag nanoparticles (black), MBA concentrations from left to right are 0, 1, 10, and 50 μM. For Au nanoparticles (red), MBA concentrations from left to right are 0, 1, 10, and 50 μM. For Au nanoshells (green), MBA concentrations from left to right are 0, 50, and 500 μM. (e) Fitted peak position and width for histograms of r_{Ry} from figure 2, similar to (d). (f) Fitted peak

position and width for histograms of r_{bkgd} from bright Raman signals of parts (a), (b) and (c).

SERS-CS detects a polarization response and rotational diffusion times

The temporal response of SERS from individual nanoparticles may be analyzed using correlation spectroscopy, similar to fluorescence correlation spectroscopy (FCS) [9]. The correlation response in SERS experiments on diffusing nanoparticles often show two time scales (Figure 4a). The longer time scale is from translational diffusion of the nanoparticles through the confocal detection volume, and the shorter time scale is from rotational diffusion of the nanoparticles. The rotational diffusion is visible if the Plasmon resonance of the nanoparticle is preferentially excited along a certain direction. Such a preferred direction may arise due to varying shapes of particles or by inter-particle junctions. For truly spherically symmetric particles, no sensitivity to polarization is expected.

When the laser excitation is polarized along the preferred dipole of a nanoparticle or nanoparticle assembly, a larger scattering signal is observed. In addition, the detection efficiency is sensitive to polarization either by design (using a polarization sensitive element on the detection path) or by necessity (the objective will detect light polarized along the optical axis much less efficiently). We split the emission into two perpendicular polarizations, and monitor the fluctuation time scales by performing auto- and cross-correlations between the two signals. Since a particle cannot be scattering strongly into the two perpendicular polarizations, we expect cross-correlations between the two channels to show reduced or negative amplitude for the shorter time scale, if it is indeed from rotational diffusion of the nanoparticles. Figure 4a does indeed show such reduced amplitudes, supporting our identification of the rotational and translational diffusion time scales. Similar rotational diffusion measurements were seen previously with spherical Ag nanoparticles [9].

The three nanoparticles samples we studied show distinct characteristics when monitored with correlation spectroscopy. Applying recently developed single-molecule FCS [13] to SERS, we study the correlations from individual nanoparticles or nanoparticle clusters. In Figures 4b-d, we show examples of the autocorrelations of the Rayleigh (red) and the Raman (black) channels as well as their cross-correlations (green and blue) for individual nanoparticles or nanoparticle clusters. In all cases, autocorrelations and cross-correlations of the Raman and Continuum Background channels overlap within expected error.

Figure 4b shows typical results for particle assemblies of Ag nanoparticles. Both the Raman (black) and Rayleigh (red) channel autocorrelations show strong rotational diffusion contributions, and the cross-correlations show similar contributions, indicating that the Rayleigh and Raman dipoles are at least roughly aligned.

The Au nanoparticles have a different behavior. First, the amplitudes of the rotational diffusion components are smaller than for the Ag nanoparticles in the autocorrelations. Second, the cross-correlations often have negative amplitudes, indicating that strongest dipole directions for the Rayleigh and Raman scattering may not overlap. These two facts may indicate that there are multiple strong scattering interfaces in each nanoparticle assembly, with one stronger for the Rayleigh signal and another stronger in the Raman signal.

The Au nanoshells show a third, very important behavior (Figure 4d). The rotational diffusion component of scattering is not detectable in most cases. This is what is expected for a spherically symmetric, scattering nanoparticle. A previous study claimed that the rotational diffusion component could be seen with individual, spherically symmetric nanoparticles [9]. We were not able to observe SERS scattering from solid nanoparticles without some aggregration [14].

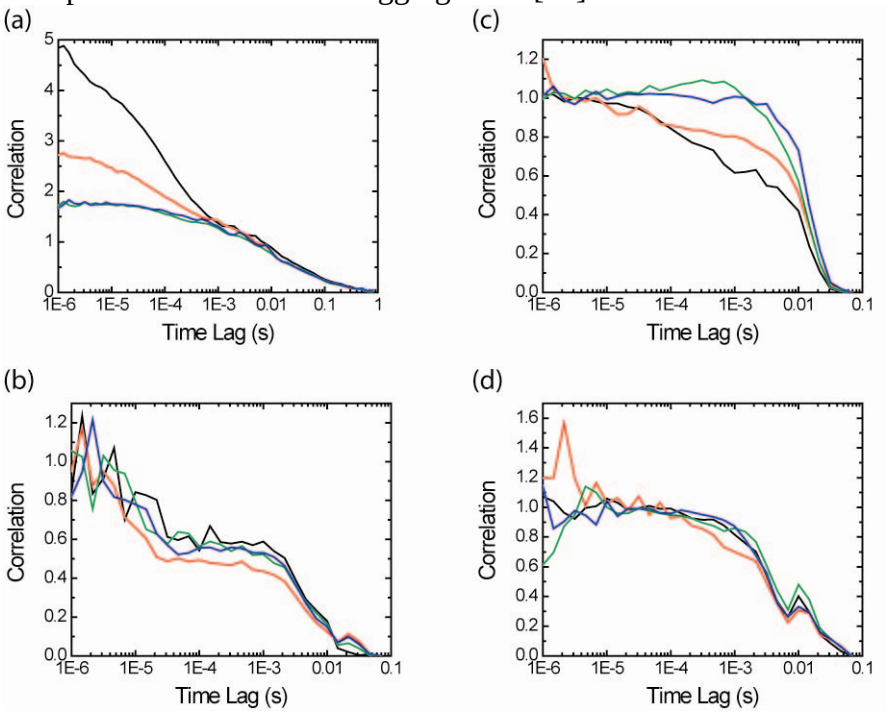

Figure 4: (a) Scattering from nanoparticles are monitored using two channels, one with polarization parallel to the excitation, and one perpendicular to the excitation. Autocorrelations of the parallel (black) and perpendicular (red) channels are shown, as well as cross-correlations of the two channels (green and blue). There are two timescales of fluctuations evident. The longer timescale is from translational diffusion and does not depend on polarization. The shorter timescale is from rotational diffusion. The ability to detect rotational diffusion depends on the anisotropic polarization dependence of plasmon excitations due to clustering of nanoparticles. For nanoshells, the rotational diffusion fluctuations are absent due to the isotropic plasmon resonance. Using the information that the second correlation timescale is due to rotational diffusion, we can study the relative orientation of Raman-active and Rayleigh-active dipoles in samples. Representative correlations from *single bursts* are shown after expanding the correlation region [13]. (b) Correlation for single Raman active Ag scattering center. Autocorrelation of Raman signal (black), autocorrelation of Rayleigh signal (red), and the two cross-correlations of the Raman signal with the Rayleigh signal (green and blue) are shown. (c) Correlations for single Raman active Au scattering center. (d) Correlations for single Au nanoshell.

In Figure 5, we show histograms of fitting parameters for the correlations obtained for each nanoparticle observed in the experiments described earlier. For each nanoparticle or cluster, three fitting parameters are shown: the translational diffusion time , the rotational

diffusion time, and the ratio of the rotational diffusion correlation amplitudes of the cross-correlations to that of the autocorrelation. The results for the Ag nanoparticles are on the left (Figures 5a-c), those for the Au nanoparticles are in the middle (Figures 5d-f), and those for the Au nanoshells are on the right (Figures 5g-i). In each case, histograms are shown for increasing MBA concentration from black, to red, to green.

Green histograms in (a), (b), and (c) have longer timescales, and are "spread out" all over the place, indicating aggregation. The largest peak in A_P for Ag (red and black in (c)) is for values near 0.5, indicating most of the time the Rayleigh and Raman dipoles are aligned. For the Au (b), most of the time the dipoles are not aligned. Note that the width of the peak for A_P is larger for Au (b) than for the nanoshells, even though the signals are more intense in the case of Au.

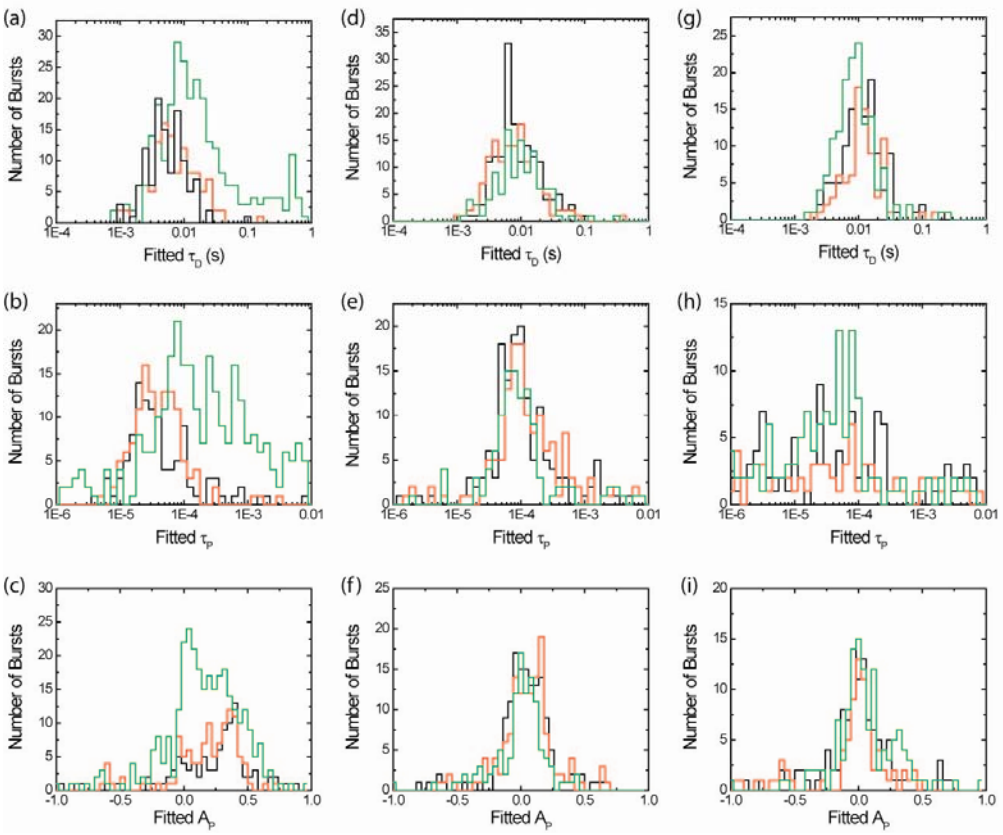

Figure 5: For each scattering center, a two component correlation spectroscopy model is fitted to the correlations from the burst of photons. It is a global fit for all four correlations shown in figure 4. The results are formed into histograms shown here, and the populations are fitted. Histograms for Ag nanoparticles with 0 (black), 10 (red), and 50 μM MBA (green) are shown for fitted diffusion time τ_D (a), fitted time scale for polarization-related fluctuations (b), and the relative amplitude A_P of the polarization-related fluctuations for the cross-correlations (c). Histograms for Au nanoparticles with 0 (black), 10 (red), and 50 μM MBA (green) are shown in (d), (e), and (f), similar to (a), (b), and (c). Histograms for Au nanoshells with 0 (black), 50 (red), and 500 μM MBA (green) are shown in (g), (h), and (i), similar to (a), (b), and (c). If A_P is larger than 0, then there was a significant component of the polarization-related fluctuation found. If A_P is less than 0, that component was negative,

Manuscript in preparation: excerpt from "Rapid monitoring of pH microenvironments using SERS"

The pH is obtained from the SERS signal by calculating the ratio of a Raman line dependent on pH to a Raman line independent of pH. We have developed a rapid assay that focuses only on the relevant lines, allowing higher throughput in the number of particles analyzed (Figure 3). Fast pH measurements are tested by scanning confocal beam in solution containing MBA-coated silver nanoparticles. For each "burst" of photons (approximately 20 ms long), the ratio of the photons detected from the pH-variable line to the total number of photons detected is calculated, and placed in the histogram to the right. There is a clear shift in this ratio when the pH of the solution is changed from pH 8.5 to pH 5.5. The widths of the peaks in the histograms are similar to those found using the full spectroscopy in [14].

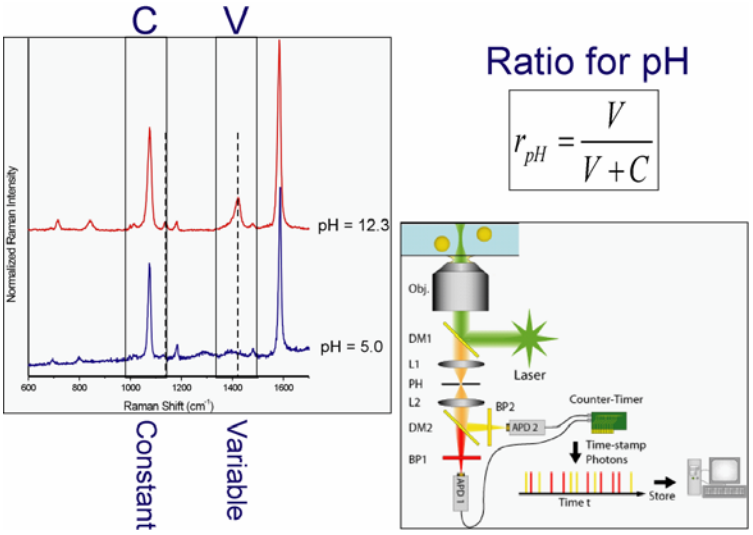

Figure 6: To measure pH using SERS, we select a Raman line that varies with pH (detector 1; selected using bandpass filter BP1) and on a Raman line that is constant (detector 2; selected using BP2). Confocal fluorescence microscopy is used to detect scattering particles; fast avalanche photodiodes (APD1 and APD2) are used to detect the scattered photons.

Figure 7 shows results of these measurements, demonstrating the dependence of the ratio on pH. The widths of the peaks demonstrate present resolution limits in our ability to determine the pH. These resolution limits are not related to the signal to noise of the measurements, but are intrinsic variations between particle clusters.

Figure 8 shows the results of combining the use of fast pH detection with a confocal scanning image. Rather than requiring 20 s per particle, the image can obtain information on hundreds of particles in 200s.

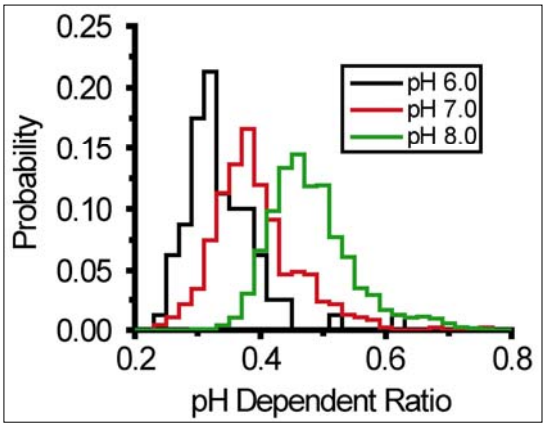

Figure 7: Histogram of pH dependent ratio $r_{pH} = V/V + C$ for many nano-pH meters diffusing in solution. The x axis is the ratio of the pH dependent line to the sum of the pH dependent and pH independent lines.

200 second, 100X100 micron scan

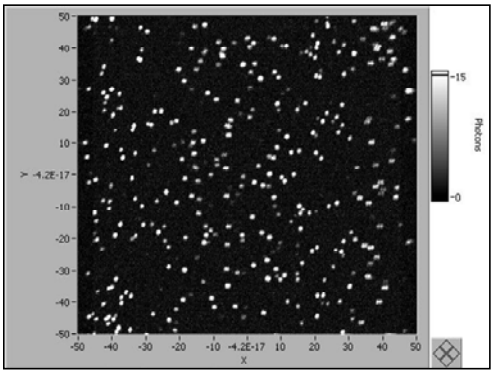

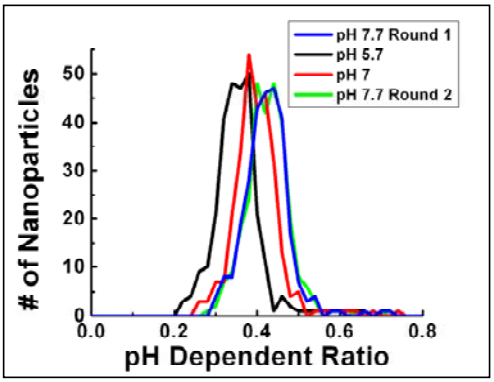

$$r_{pH} = \frac{V}{V + C}$$

Figure 8: A 200 s, 100X100 micron scan of gold nanoparticles attached to a glass surface. The ratios obtained for the particles have similar errors to those from previous pH nanoprobe measurements [14].

Invited talks

Laurence, T.A, C. Talley, T. Huser, M. Colvin, “Application of SERS Nanoparticles to Intracellular pH Measurements”, ACS Western Regional Meeting, Sacramento, October 2004.

Laurence, T.A., “Revealing heterogeneity in biological systems using single-molecule fluorescence spectroscopy and surface-enhanced Raman spectroscopy”, University of Southern California, Los Angeles, August 2004.

Laurence, T.A, C. Talley, T. Huser, M. Colvin, “Application of SERS Nanoparticles for Intracellular pH Measurements”, International Symposium on Optical Science and Technology (SPIEs 49th Annual Meeting), Denver, August 2004.

Patent application

U.S. patent application 10/935783 on "Nanosensors Based On Functionalized Nanoparticles And Surface Enhanced Raman Scattering", September 2004.

Exit Plan

This research will be continued as a collaboration with the Center for Biophotonics Science and Technology (CBST) at UC Davis Medical Center, Dr. Christine Orme at LLNL, and Tammy Olson, a UCSC graduate student working at LLNL on a SEGRF fellowship. We will be studying the effects of osteoclasts, a group of cell types that dissolve bone minerals using acidic environments, on their extracellular environment. External funding such as NIH will be sought in this collaboration. The effort to incorporate pH nanoprobes in tumor cells will also be continued as a collaboration with CBST.

References

1. Gillies, R.J., N. Raghunand, G.S. Karczmar, and Z.M. Bhujwalla, *MRI of the tumor microenvironment.* J Magn Reson Imaging, 2002. **16**(4): p. 430-50.
2. Martin, M. and L. Lindqvist, *The pH Dependence of Fluorescein Fluorescence.* J Luminescence, 1975. **10**: p. 381.
3. Lewis, I.R. and H.G.M. Edwards, *Handbook of Raman spectroscopy: from the research laboratory to the process line*. 2001, New York: Marcel Dekker. xiii, 1054.
4. Pettinger, B., A. Tadjeddine, and D.M. Kolb, *Enhancement in Raman Intensity by Use of Surface-Plasmons.* Chemical Physics Letters, 1979. **66**(3): p. 544-548.
5. Kneipp, K., Y. Wang, H. Kneipp, L.T. Perelman, I. Itzkan, R. Dasari, and M.S. Feld, *Single molecule detection using surface-enhanced Raman scattering (SERS).* Physical Review Letters, 1997. **78**(9): p. 1667-1670.

6. Michalet, X., T.D. Lacoste, and S. Weiss, *Ultrahigh-resolution colocalization of spectrally separable point-like fluorescent probes.* Methods, 2001. **25**(1): p. 87-102.
7. Schwartzberg, A.M., T.Y. Olson, C.E. Talley, and J.Z. Zhang, *Synthesis, characterization, and tunable optical properties of hollow gold nanospheres.* J Phys Chem B Condens Matter Mater Surf Interfaces Biophys, 2006. **110**(40): p. 19935-44.
8. Schwartzberg, A.M., T.Y. Oshiro, J.Z. Zhang, T. Huser, and C.E. Talley, *Improving nanoprobes using surface-enhanced Raman scattering from 30-nm hollow gold particles.* Anal Chem, 2006. **78**(13): p. 4732-6.
9. Eggeling, C., J. Schaffer, C.A.M. Seidel, J. Korte, G. Brehm, S. Schneider, and W. Schrof, *Homogeneity, Transport, and Signal Properties of Single Ag Particles Studied by Single-Molecule Surface-Enhanced Resonance Raman Scattering.* Journal of Physical Chemistry A, 2001. **105**(15): p. 3673-3679.
10. Kapanidis, A.N., N.K. Lee, T.A. Laurence, S. Doose, E. Margeat, and S. Weiss, *Fluorescence-aided molecule sorting: analysis of structure and interactions by alternating-laser excitation of single molecules.* Proc Natl Acad Sci U S A, 2004. **101**(24): p. 8936-41.
11. Moskovits, M., *Surface-Enhanced Spectroscopy.* Reviews of Modern Physics, 1985. **57**(3): p. 783-826.
12. Dahan, M., A.A. Deniz, T. Ha, D.S. Chemla, P.G. Schultz, and S. Weiss, *Ratiometric measurement and identification of single diffusing molecules.* Chemical Physics, 1999. **247**(1): p. 85-106.
13. Laurence, T.A., Y. Kwon, E. Yin, C.W. Hollars, J.A. Camarero, and D. Barsky, *Correlation Spectroscopy of Minor Fluorescent Species: Signal Purification and Distribution Analysis.* Biophys J, 2007. **in press**.
14. Talley, C.E., J.B. Jackson, C. Oubre, N.K. Grady, C.W. Hollars, S.M. Lane, T.R. Huser, P. Nordlander, and N.J. Halas, *Surface-enhanced Raman scattering from individual au nanoparticles and nanoparticle dimer substrates.* Nano Lett, 2005. **5**(8): p. 1569-74.